PAPER • OPEN ACCESS

Evaluation and validation of radial impurity density profiles from CXRS using neutral beam modelling in W7-X

To cite this article: T Romba *et al* 2023 *Plasma Phys. Control. Fusion* **65** 075011

View the article online for updates and enhancements.

Evaluation and validation of radial impurity density profiles from CXRS using neutral beam modelling in W7-X

T Romba[1,*], F Reimold[1], R J E Jaspers[2], A J Edmondson[3], O P Ford[1], B Geiger[3], S Jabłoński[4], M Kubkowska[4], T W C Neelis[2], P Zs Poloskei[1], L Vanó[1], T Klinger[1] and the W7-X Team[5]

[1] Max-Planck-Institut für Plasmaphysik, 17491 Greifswald, Germany
[2] Eindhoven University of Technology, 5612 AZ Eindhoven, The Netherlands
[3] University of Wisconsin-Madison, Madison, WI, United States of America
[4] Institute of Plasma Physics and Laser Microfusion, Hery 23, 01-497 Warsaw, Poland

E-mail: thilo.romba@ipp.mpg.de

CrossMark

Abstract

Absolute radial impurity density profiles in the Wendelstein 7-X stellarator (W7-X) are derived from charge exchange recombination spectroscopy using modelling of the neutral beam. The approach is validated via cross comparisons of the neutral beam attenuation, the radial localization of ion temperature measurements, as well as a comparison of the effective plasma charge determined by other diagnostics. The latter implies the validity of the obtained absolute density levels. The simulation based approach novel to W7-X allows to assess the neutral beam halo population, introducing corrections to the shape and amplitude of determined impurity density profiles. To illustrate the capabilities of the derived impurity density profiles, the particle transport properties in a W7-X discharge heated by electron cyclotron resonance heating were assessed. Density profiles for various impurities are found to be flat, consistent with dominant anomalous diffusion in the range 0.1–$5.0 \, \mathrm{m^2 \, s^{-1}}$. This range of the anomalous transport in such plasmas is in line with other impurity diagnostics at W7-X.

Keywords: impurity transport, Wendelstein 7-X, charge-exchange-recombination-spectroscopy

(Some figures may appear in colour only in the online journal)

1. Introduction

The monitoring of the impurity content in the confined plasma of a fusion reactor is essential due to the detrimental effects of large impurity populations on the plasma performance.

High concentrations of low Z impurities, such as the fusion ash helium, decrease the fusion power via dilution of the hydrogen fuel. High Z impurities increase the power losses from the plasma via line-radiation and strong bremsstrahlung from the plasma core and reduce the energy confinement [1]. To avoid such detrimental impurity concentrations in future reactor plasmas, the transport behaviour of impurities from their respective source location and within the plasma needs to be understood.

Plasma impurities originate either from the fusion reaction in the core (helium) or from outside the last closed flux surface (LCFS) in case of all other impurities. Regardless of the source location, different transport channels will distribute the

impurities across the full plasma volume. The radial transport of impurities in the confined plasma can be described by an effective diffusive transport component, D, scaling with local density gradients, and an effective convective transport component, v, scaling with the local density. In cylindrical approximation, this reads:

$$\frac{\partial n_z}{\partial t} = \frac{1}{r}\frac{\partial}{\partial r} r\left(D \cdot \frac{\partial n_z}{\partial r} - v \cdot n_z\right) + S_z, \tag{1}$$

where $r = \sqrt{V/(2\pi^2 R_{\mathrm{axis}})}$ denotes the minor radius of a flux surface enclosing a volume V at major plasma radius R_{axis}, n_z the local impurity density in a given charge state, z, at time t, and S_z denotes sources and sinks of the respective ionization state of the impurity. In the following, ρ, the effective minor radius r_{eff} normalized to the minor plasma radius a, is used as the radial coordinate.

To assess the impurity transport experimentally, various measurement techniques are available. Using laser-blow-off (LBO) [2] or tracer-encapsulated-solid-pellets (TESPEL) [3], local impurity transport properties are derived from spectroscopic signatures induced by active impurity injection. Radial fluxes of high Z impurities can be obtained using x-ray imaging crystal spectroscopy (XICS) [4]. Charge exchange recombination spectroscopy (CXRS) [5] is used to measure full radial profiles of low and medium Z impurities without the need for an error-prone inversion as needed for XICS.

In the following, a framework for a CXRS based evaluation of impurity densities in the optimized stellarator Wendelstein 7-X (W7-X) [6, 7] is introduced. In section 2, the theory behind CXRS and the necessary input parameters for the framework are introduced. The framework is validated in section 3 via cross comparison with other diagnostics. As an exemplary application case, section 4 presents an assessment of the compatible impurity transport coefficients in case of a W7-X program heated by electron cyclotron resonance heating (ECRH) based on steady-state radial impurity density profiles.

2. Methods

The CXRS system of W7-X was successfully set up and used for impurity density analysis in the experimental campaign OP1.2b at W7-X [8, 9]. The system is also routinely used to derive radial profiles of the ion temperature.

Charge exchange radiation originates from the relaxation of a bound electron after the transfer to a (partially) ionized atom during a charge exchange reaction:

$$H + A^{z+} \rightarrow H^+ + A^{(z-1)+,*}, \tag{2}$$
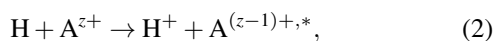
where H denotes hydrogen as the charge donating species, A^{z+} denotes an impurity ion of charge z, and an asterix refers to a bound electron in an excited state. The radiation emitted by the relaxation of the electrons is proportional to the impurity density in the initial ionization state z, $n_{A^{z+}}$, and the local donor

density n_0. With the connected effective reaction rate $\langle\sigma v\rangle_{\mathrm{eff}}$, the intensity of the charge exchange emission scales like:

$$I_{\mathrm{CX}} \propto n_0 \cdot n_{A^{z+}} \cdot \langle\sigma v\rangle_{\mathrm{eff}}. \tag{3}$$

Due to the high temperatures in the confined region of a fusion plasma compared to the ionization energy of hydrogen, CXRS emission from the confined plasma region is fairly weak. To facilitate measurements within this region nonetheless, an artificial increase in the local neutral density is imposed. Local puffing of neutral gas at the plasma edge [10] or the injection of neutrals by neutral beams injection (NBI) [5] increase n_0 locally, leading to localized charge exchange (CX) emission. The selection of suited observation volumes then allows to assess local impurity densities throughout the whole radial coordinate.

In case of NBI, ions are accelerated outside the reactor, neutralized, and subsequently injected into the plasma. Due to the strong spatial localization of the beam accompanied by the beam induced signal being orders of magnitudes larger than the background CXRS signal, the measurement region of the CXRS emission is restricted to the intersection region of the neutral beam and the spectroscopy lines of sight (LoS).

The radiation originating from beam induced reactions is commonly referred to as the active component of the CXRS signal. This component is accompanied by a so called passive component which is caused by electron, or ion impact excitation, recombination events, or charge exchange reactions with thermal background neutrals. The passive component is typically weaker for high Z impurities. It is present regardless of beam operation, allowing to separate the two components by a temporal modulation of the beam [8].

Besides a temporal separation, the active and passive components can also be distinguished via their imprinted temperatures. The latter is possible as both components exhibit a temperature specific Doppler width σ:

$$\sigma = \lambda_0\sqrt{\frac{eT_{\mathrm{app}}}{m_i c^2}}, \tag{4}$$

where λ_0 denotes the transition wavelength at rest, e and c the elemental charge and speed of light, respectively, T_{app} the apparent ion temperature, and m_i the ion mass. Note that the apparent temperature of the Gaussian line shape is larger than the real ion temperature due to instrument function and fine structure effects [11].

The neutral population injected by NBI is found to consist of three components separated in energy [12]. These components originate from H^+, H_2^+, and H_3^+ ions being formed in the source plasma of the beam. Acceleration of these ions by an acceleration voltage of around 56 keV in the W7-X case [13], gives rise to three neutral density populations with energies matching the full, a half, and a third of the acceleration voltage. As the charge exchange cross section depends on the relative velocity of impurity ion and neutral, these components need to be treated individually when evaluating CXRS signals.

Besides these three beam based components, a fourth population of neutrals, the so-called halo component, is present

during beam operation. This population originates from charge exchange reactions between beam neutrals and main ions and constitutes a thermal population of neutrals with dependencies on the local ion and electron temperature as well as the local electron density [14]. The halo based emission was estimated to cause up to 35% of the active charge exchange signal in case of the ASDEX Upgrade tokamak (AUG) [14].

The reaction rate of a CX reaction strongly depends on the excited state n of the neutral as the energy levels in the donor and acceptor atoms need to be similar. In case of reactions involving beam neutrals, the reactions rates with neutrals in the $n = 1$ excited state are the dominant contribution to the CXRS signal [14]. In contrast, the CX cross section in the halo case is highest for neutrals in the $n = 2$ excited state, making it necessary to treat the neutral density in an excited state resolved manner.

Accounting for the four different energy components E, the respective excited states, and the measurement being line integrated, any CX signal can be generally expressed as

$$I_{\text{meas}} = \frac{1}{4\pi} \int_{\text{LoS}} \underbrace{\sum_{E=1}^{4} \sum_{n} n_z(l) \cdot n_{0,E,n}(l) \cdot \langle \sigma_{E,n} v \rangle_{\text{eff}}(l)}_{\varepsilon_{\text{CX}}}$$

$$+ \, \varepsilon_{\text{passive}} \, dl, \tag{5}$$

where $n_z(l)$ is the impurity density of the probed charge state at location l, $n_{0,E,n}(l)$ is the density of beam component E at location l in excited state n with the corresponding effective reaction rate given by $\langle \sigma_{E,n} v \rangle_{\text{eff}}(l)$. ε_{CX} is the local active charge exchange emissivity while $\varepsilon_{\text{passive}}$ relates to the passive emissivity from the plasma edge.

2.1. Neutral density simulation

To resolve the various dependencies of equation (5), measured charge exchange intensities can be analysed using the beam emission spectrum [15]. While this approach allows to simplify the analysis significantly in various aspects, it has the drawback of not accounting for local variations in the plasma parameters along the integration path and typically does not account for halo based emission.

In order to properly resolve the integration of equation (5), the neutral densities need to be known space and state resolved. A way to obtain such information is by means of neutral transport modelling of the neutral beam [14]. In case of simulated neutral densities, the integration of equation (5) changes to a summation over all grid cells crossed by the given LoS with the active part of the emission being given by:

$$I_{\text{act}} = \frac{1}{4\pi} \sum_{C} \sum_{E=1}^{4} \sum_{n} n_z(C) \cdot n_{0,E,n}(C) \cdot \langle \sigma_{E,n} v \rangle_{\text{eff}}(C)$$

$$\cdot \, \Delta L(C), \tag{6}$$

where C relates to all cells passed by a given LoS with $\Delta L(C)$ being the respective intersection length of cell and LoS.

The feasibility of simulated neutral densities in context of CXRS signals was shown in the AUG case [14] using the FIDASIM code [16]. In the following, the python version of this code, pyFIDASIM [17], is used to simulate neutral densities based on experimentally determined plasma profiles and beam parameters. Neutrals are simulated up to the $n = 6$ excited state. Simulations are performed with 50 000 markers per active source, relating to a runtime of 20 min per source per assessed time window.

2.1.1. Neutral beam parameters. The neutral beam input parameters necessary to simulate the beam attenuation are the beam geometry, the total beam power, the acceleration voltage, and the fractions of the beam in the three energy components. At W7-X all these parameters are routinely measured and available from the experimental database [18]. The nominal beam power exceeds the power coupled to the plasma due to scraping of the beam by the port, beam attenuation outside the LCFS, and beam shine through. Based on the observations discussed in section 3.1, the nominal NBI power is down scaled by a factor of 0.7 in the following. The allocation of the beam power to the different beam components is based on neutralizer spectroscopy in the neutral beam source. For the cases assessed in the following, the beam power fractions are found to 0.3, 0.52, and 0.18 in the full, half, and third component, respectively.

2.1.2. Plasma profiles. The plasma profile information needed to determine the local charge exchange reaction rates and to simulate the beam attenuation includes the electron density as well as the electron and ion temperatures. All ion species are described by a joint ion temperature as the temperatures of the various species equilibrate by collisions between the different ions.

Electron density and temperature profiles are determined using the Thomson scattering system of W7-X [19]. The ion temperature is derived from the Doppler width of the carbon CXRS emission [8]. As the CXRS based T_i measurement is error-prone near the plasma edge and the electron and ion temperatures are expected to be similar due to high collisionality in this region [8], the ion temperature outside $s = \rho^2 = 0.6$ is determined using the Thomson scattering data points exclusively. Radial profiles are obtained using a Nadaraya–Watson regression [20], giving rise to continuous profiles ranging from $\rho = 0.0$ to $\rho = 1.0$. To improve the match between simulated and measured beam attenuation, the plasma outside the LCFS is neglected in the simulation by setting the plasma density to $1 \, \text{m}^{-3}$.

Radially resolved profiles of the effective plasma charge $Z_{\text{eff}} = \left(\sum_i n_i Z_i^2 \right) / \left(\sum_i n_i Z_i \right)$ are calculated iteratively from the determined impurity density profiles. An iterative approach is necessary as the beam-halo charge exchange reaction rate scales with the local main ion density. Furthermore, charge exchange with impurity ions is accounted for as a sink of the beam neutrals. Within the simulation, carbon is assumed to be

the only present impurity, accounting for the whole $Z_{\rm eff}$. The simulation and calculation loop is repeated until convergence in the $Z_{\rm eff}$ profile is obtained.

2.1.3. Rate data. For the effective charge exchange rate data $\langle \sigma v \rangle_{\rm eff}$, a data set compiled for AUG is used [14]. The rate data for the argon transition in use is corrected for by the corrections listed in [21] for the transition at 541.09 nm. Due to the energy range of the W7-X NBI, this correction reduces to a re-scaling of the rate data by a factor of 2.73. The rates calculated for the AUG case are applicable in case of W7-X due to the comparable ranges in $E_{\rm beam}$, $n_{\rm e}$, $T_{\rm i}$, and $Z_{\rm eff}$.

The rate data in case of the beam components spans a four dimensional parameter space in electron density, ion temperature, injection energy, and effective plasma charge $Z_{\rm eff}$. In case of halo emission, the number of dimensions reduces to three as the rates no longer depend on the injection energy as the neutrals do not exhibit a collective motion relative to the isotropic plasma particles. Rates for a given set of plasma parameters are calculated using multivariate interpolation in the respective multi-dimensional parameter space with the relative error in the rate data assumed to be 10%.

2.1.4. Impurity density calculation. Using a measured intensity, $I_{\rm meas}$, the local impurity density $n_z(C)$ remains as the sole unknown in equation (6). To resolve the radial dependency and thus be able to separate the impurity density from the summation, a functional shape for $n_z(C)$ needs to be assumed. The observation volumes are strongly localized by the intersection of beam and LoS. Hence, n_z is assumed to be constant along a given LoS in the following. While this approximation is applicable in regions of flat n_z profiles, especially in gradient regions near the edge, systematic errors may be introduced.

To account for a finite width of observation volumes, the weights of the contributing cells are determined as the average of four LoS arranged in a circle of 1 cm radius around the nominal LoS. This correction was found to improve results for AUG H-mode data with pedestals [14]. It is found to only have an insignificant influence on the results in the analysed W7-X case however.

2.2. CXRS system

The optical system in use for CXRS in W7-X is composed of three spectrometers [8]. The spectrometer used for the analysis of the H_α beam emission, the main impurity carbon, as well as the fusion ash helium is an ITER-like-spectrometer (ILS) [22] with 54 fibres. The three separate channels of the spectrometer are referred to as red, green, and blue in the following due to the wavelength regions of the respective transitions. The C^{5+} emission is probed to assess the fully ionized carbon content. A Ne^{9+} emission line is within the wavelength range of the green channel, allowing for an assessment of the fully ionized neon density without the use of an additional spectrometer. Two additional, variable wavelength spectrometers with 45 channels each, referred to as AUG1 and AUG2 in the

Table 1. Overview of the relevant CXRS transitions as measured in OP1.2b of W7-X.

Species	Transition	Wavelength	Spectrometer
H	$n = 3 \rightarrow 2$	656.28 nm	ILS_Red
B^{4+}	$n = 7 \rightarrow 6$	494.47 nm	AUG 1 & 2
C^{5+}	$n = 8 \rightarrow 7$	529.06 nm	ILS_Green, AUG 1 & 2
N^{6+}	$n = 9 \rightarrow 8$	566.95 nm	AUG 2
O^{7+}	$n = 10 \rightarrow 9$	606.85 nm	AUG 1
Ne^{9+}	$n = 11 \rightarrow 10$	524.49 nm	ILS_Green
Ar^{15+}	$n = 14 \rightarrow 13$	436.52 nm	AUG 2

following, are also available. An overview of the various transition lines measured by the different spectrometers is given in table 1.

The available spectrometers are connected to four LoS arrays that intersect the beam at ρ values from 0.1 to 1 (LCFS). Two of these arrays cross one of the commissioned neutral beam sources 7 and 8 from top to bottom under a 45° angle in the poloidal direction each (AEM21_S7 and AEM21_S8, respectively). Another array (AEA21_A) is oriented toroidally, crossing both neutral beam sources. The fourth LoS array (AET) is oriented poloidally under an angle of 45° but originates from the bottom of the machine. The ILS spectrometer is connected to 19 AEA21_A, 6 AET, as well as 10 AEM21_S7 and AEM21_S8 LoS each. Both of the AUG type spectrometers are connected with 24, 10, and 9 channels to the AEA21_A, AEM21_S7, and AEM21_S8 arrays, respectively. For details of the LoS geometry and the relative location of the NBI, see figures 1 and 2 in [8]. Due to inferior data (signal-to-noise-ratio) from the AET LoS, the related data is not analysed in the following.

The intensity of the active CXRS emission is post-processed in line with the beam operation mode. In case of beam blips with typical lengths of 20 ms, frames identified to overlap with beam operation are summed over with typical frame times of 10 ms. The passive background emission spectrum is defined as the average of the five preceding and five succeeding frames which do not overlap with beam operation. It is subtracted from the total signal during the beam phase. The so obtained active intensity is rescaled by the ratio of the total frame time to beam operation time. This compensates for frames only partially illuminated by the beam blip.

In the opposing case of continuous beam operation, background subtraction is not applicable due to the lack of reference frames without beam. In this case, the spectra are fitted using the sum of a low temperature component mimicking the integrated edge emission and a high temperature component relating to the active emission. The cold component is fitted using a super Gaussian ($\propto \exp[-(\Delta\lambda/\sigma)^{2\beta}]$) with β in the range $[0.6, 2.0]$. This functional shape is found to match the shape of the passive component superior relative to a normal Gaussian. This is presumably caused by integration effects in the cold plasma edge due to the scaling of the Doppler width with $\sqrt{T}$. The active CX intensity $I_{\rm act}$ is then deduced from the high temperature Gaussian fit. Uncertainties in the intensity

arise from the absolute intensity calibration and are assumed to 10% in the ILS and 20% in the AUG cases, respectively.

Regardless of the beam operation scheme in use, all ions are expected to be described by a unique temperature. This allows to reduce the number of degrees of freedom in the fit by determining the local ion temperature from one species and enforcing it onto the others. Within this procedure, effects altering the apparent temperature need to be accounted for [5]. To determine the ion temperature associated with a given LoS, a spectrum of a reference species is fitted with a Gaussian of free width first. The obtained T_i is then down-corrected by a correction factor accounting for fine structure as well as instrument function effects where the instrument function is assumed to be of super-Gaussian type. The so-obtained T_i is then enforced in the spectral fits of the other impurities at same ρ using the correction loop in the opposite direction, accounting for the transition specific fine-structure and the instrument function of the respective spectrometer.

In W7-X, carbon is suited to determine the ion temperature due to its typically high concentration originating from it acting as the first wall material. In case of neon being present in the system, neon rather than carbon needs to be used to derive the reference temperature as neon emission in the flanks of the carbon signal distorts the carbon temperature measurement. Using knowledge of the radial locations of the various LoS, the measured reference temperatures are interpolated to the LoSs of the other spectrometers to enforce the width of their active component.

3. Validation

The following chapter depicts a validation of the previously introduced CXRS analysis framework based on comparisons with other diagnostics. To assess the beam attenuation as well as changes in the effective plasma charge, the Nitrogen seeded discharge 20180920.049 is assessed in the following. An overview over the central discharge parameters is given in figure 1. The discharge corresponds to a hydrogen plasma heated by 4 MW of ECRH with four diagnostic CXRS blips of length 20 ms present. The magnetic field corresponds to the W7-X standard configuration with an on-axis magnetic field of 2.52 T. Electron temperature profiles are slightly peaked with line integrated densities around $8 \times 10^{19}\,\mathrm{m}^{-3}$. Nitrogen is seeded starting at $t = 4\,\mathrm{s}$ with two different flow rates as apparent by the slope in the radiated power. Ion temperatures are found to obey the ion-temperature-clamping limit in W7-X [23]. The significant scatter in the Thomson based data points is caused by hardware problems in the profile diagnostic.

3.1. Beam attenuation

The central metric when modelling neutral beam densities is the attenuation of the injected neutral populations within the plasma. The best suited experimental parameter to assess the beam density at various radial locations is the H_α beam emission signal (BES) at 656.28 nm. This signal originates
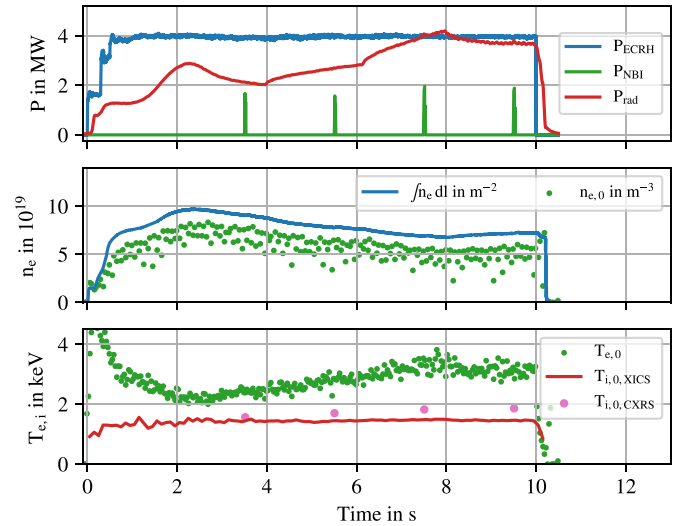
Figure 1. Overview plot of the main plasma parameters of W7-X program 20180920.049.
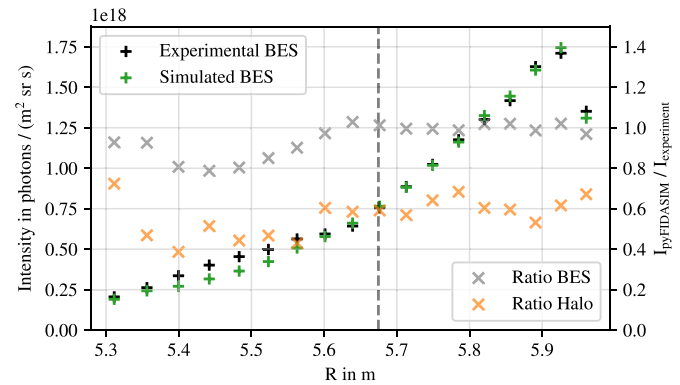
Figure 2. Comparison of simulated and measured integrated beam emission and halo signals for an NBI blip of source 8 only. The projection of the major radius at a toroidal angle of 95° is given by the dashed vertical line.

from excitation of the beam neutrals by the plasma. It contains Doppler shifted emission originating from the three beam components as well as the unshifted halo radiation. The respective intensities scale linearly with the neutral density of the respective components. The simulated neutral density allows to calculate synthetic BES signals using the imposed plasma profiles. By direct comparison of the line integrated intensities of the experimental and synthetic emission, the quality of the simulated beam attenuation can be assessed.

In figure 2, such a comparison in case of W7-X program 20180920.049 is displayed. The nominal beam power is down-corrected by a multiplicative factor of 0.7 to account for a better match between simulation and experimental data. The general shape of the beam attenuation ($+-$shaped markers) is well matched by the simulated intensities. The simulation under-predicts the emission slightly on the inboard side and matches the emission well on the outboard side. In case of the measured data points on the inboard side inside $R = 5.6\,\mathrm{m}$, a change in slope is present within the experimental data

which is not reproduced by the simulation. This deviation is expected to originate from line integration effects originating from the three-dimensional geometry of W7-X. It is observed throughout the available NBI data set, regardless of magnetic configuration or NBI operation type, hinting towards systematic shortcomings in pyFIDASIM when applied to W7-X. As measured CXRS intensities of the impurities are found to follow the same trend on the inboard machine side, these data points are discarded in the following. This is necessary as the discrepancy between simulated and experimental neutral densities would introduce systematic deviations when used within the analysis.

The discrepancy in beam attenuation is also apparent in the ratio data (x-shaped markers) of figure 2. The figure displays the relative intensities of synthetic and experimental intensity in the BES and halo case. While the relative strength of simulated and measured BES signal is close to unity for all data points, it becomes apparent that the halo density is systematically under-predicted by the simulation by up to 40% in the relevant region. Besides not accounted for sources of halo neutrals in the simulation, this underestimation may be caused by an underestimated $E/3$ fraction of the neutral beam. For this component, the CX cross section with thermal ions is higher than for the other components while the power per particle is low. These two effects combined allow for an increase in halo neutrals by means of more particles in the $E/3$ component while altering the beam power only slightly.

The qualitative and quantitative match of the BES signal indicates the applicability of the pyFIDASIM code to beams in W7-X with errors in the determined neutral density being of the order of 10%. In case of the halo, the model systematically under predicts the emission, and thus density. The attenuation of the halo density is recreated well as apparent by the flat ratio in the outboard side data of figure 2 however. To compensate for the systematic underestimation of the halo density, it is divided by the observed factor of 0.6 in the following.

In the following, beam based neutral densities are assigned with a relative error of 10% while halo neutral densities are assigned with a relative error of 40%. With the halo contributing up to 40% of the measured CX emission in high density scenarios, its systematic underestimation introduces a relative error of up to 16% to the derived impurity densities. Note that the error is typically larger for NBI heated discharges due to the increased plasma density connected to the fuelling of the beam.

3.2. LoS localization

When using the BES signal to infer neutral densities from CXRS signals, the measurements are localized to the point of closest approach between LoS and beam axis. The same applies for the localization of CXRS based ion temperature measurements. While this approach is expected to localize the measurements properly in case of toroidally oriented LoS due to their slow change in penetration depth, poloidally oriented LoS which cross the flux surfaces more rapidly are expected to be localized further inside than their real emission location.
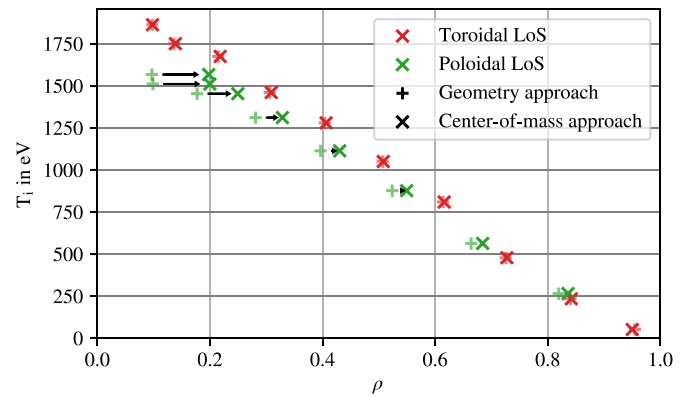

Figure 3. Ion temperature data points localized by the geometry approach ($+-$shaped markers) and the centre-of-mass approach (x-shaped markers) for toroidal and poloidal lines of sight during ECR heated W7-X program 20180920.049. Exemplary changes in the measurement locations are indicated by black arrows.

This arises as these LoS cross several flux surfaces within the beam intersection volume, giving rise to additional radiative components at larger minor radius, subsequently shifting the effective radiating component radially outward (compare figure 1 in [8]).

In case of a simulated, spatially resolved neutral density, the radial locations of the individual radiative contributions are known, allowing for a different approach to localize the measurements radially. By weighting the radial locations of the contributing cells via the normalized intensity, the corresponding centre of mass of the radiation, and thus the average emission location can be determined. The so obtained location is expected to match the real emission location better by moving poloidally oriented measurements radially outward. Assigning a radial error to the so obtained radial locations using error propagation is found to constitute no suitable metric due to the resulting errors being in the sub-millimetre range, significantly smaller than the geometric uncertainties in the system of the order of cm.

A suited proxy to check for improvements of the measurement localizations via this different approach is the ion temperature. A comparison of the ion temperature data localized using the two approaches is given in figure 3. In the $+-$shaped markers from the geometric approach, a systematic deviation between toroidal and poloidal LoS is apparent. In contrast, centre-of-mass based data given by the X-shaped markers exhibits significantly reduced systematic deviations. Changes in location near the magnetic axis are stronger than at the plasma edge due to a steeper intersection angle between LoS and flux surfaces near the plasma core. Note that the T_i values in both data sets are the same as only the radial localization is affected. Overall, the profile data hints towards the centre of mass data points as an improved metric of measurement localization for CXRS based (ion temperature) measurements. For fixed beam geometry, the effect is expected to be similar in different discharges with similar beam attenuation, allowing for a general correction of the CXRS based T_i measurement locations.
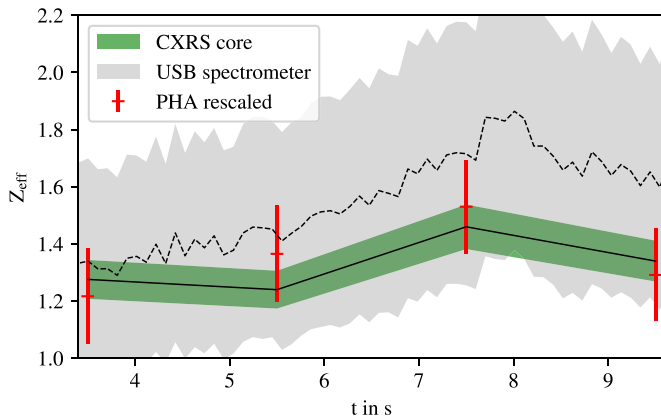
Figure 4. Comparison of the on-axis effective plasma charge from CXRS (red region) with a line averaged measurement (grey region) and data from the PHA system (purple markers) in case of plasma program 20180920.049.

3.3. Effective plasma charge scaling

To validate the absolute magnitude of the derived impurity densities, the effective plasma charge Z_{eff} can be assessed. This parameter is used as it is suited for a joint description of the known plasma impurity content. As the CXRS measurement allows to measure radially resolved profiles, radially resolved Z_{eff} values can be deduced from the measurements. In contrast to this, other diagnostics measuring the total impurity content typically measure local or LoS averaged values only.

A comparison of CXRS based and line averaged measurement of Z_{eff} is shown in figure 4 in case of experiment 20180920.049 with beam blips at four equidistant points of time. The CXRS based data points are obtained by accounting for all impurities monitored by CXRS with all assessed states being fully ionized. Nitrogen, carbon, and residual amounts of oxygen and neon were spectroscopically assessed. Nitrogen was seeded starting with the second blip giving rise to the observed increase in Z_{eff}. The grey shaded region is based on data from line averaged Z_{eff} measurements from a USB-spectrometer which deduces Z_{eff} from the bremsstrahlung background level with a temporal resolution of 100 ms [24]. The data is accompanied by the CXRS based on-axis effective charge given by the black solid line. Uncertainties in the CXRS data is obtained via error propagation and indicated by the red shaded region. Within the large error bars of the bremsstrahlung based data, the CXRS data points are well contained, indicating the validity of the absolute impurity level. Note that the comparison between the line integrated measurement and the on-axis Z_{eff} from CXRS is not strictly correct but applicable due to the large error bars of the bremsstrahlung based measurement.

A stricter comparison of the determined impurity content can be performed using data from the pulse height analysis (PHA) system at W7-X which deduces impurity densities from measured line and continuum radiation [25]. The purple data of figure 4 depicts the PHA based effective plasma charge at $\rho = 0.0$. The PHA data was reduced to the species analysed by CXRS and down-corrected to obtain the on-axis Z_{eff} value.

A down-correction is necessary as the PHA analysis assumes impurity profiles of the form $n_z \propto n_e$, with n_e profiles being typically centrally peaked in W7-X. As will be discussed in section 4, impurity density profiles in ECRH discharges are typically found to be flat, giving rise to a systematic overestimation of the PHA data points when comparing with the CXRS based on-axis Z_{eff} value. To correct for this, the PHA data points are downscaled by a factor of $\int_0^1 n_e(\rho)d\rho/n_e(0) \leqslant 1$. The so obtained data is expected to match the on-axis impurity content as determined by the CXRS system. This expectation is confirmed by the good match of the red data points of figure 4 with the CXRS data points, indicating the validity and accuracy of simulation based CXRS impurity density measurements in W7-X.

4. Application

Based on the previously introduced analysis framework, transport properties of impurities in a W7-X example case heated by ECRH are assessed. Experimental profiles are compared to simulated impurity profiles calculated by the one dimensional transport code pySTRAHL [17]. Classical and neoclassical transport coefficients used in the simulations are calculated using the NEOTRANSP code [26]. This code calculates the Maxwellian weighted average of the mono-energetic transport coefficients calculated using DKES [27, 28] at a given temperature.

Based on other diagnostics, the impurity transport in W7-X was found to be diffusion dominated in case of ECRH plasmas with $P_{ECRH} > 2\,MW$ [29, 30]. Impurity transport analysis of high Z elements showed no charge dependence of the dominant transport component [29]. LBO analysis of iron predicts anomalous diffusion levels of the order of $0.3\,m^2\,s^{-1}$ which peak near the LCFS to values of around $2.5\,m^2\,s^{-1}$ [30]. TESPEL based experiments indicate dominant anomalous diffusion of the order of $0.5\,m^2\,s^{-1}$ [31].

The analysis of transport properties in ECRH plasmas using CXRS is restricted to low frequency NBI blips as the plasma profiles may not be significantly affected by the heating aspect of the NBI. This gives rise to a low probing frequency, allowing to assess long term changes or stationary behaviour for such plasmas only.

A transport assessment in such a discharge is based on figure 5. The underlying program 20180920.049 was introduced in figure 1. In pyFIDASIM, the neutral densities are simulated with 50 000 markers per active source. Besides nitrogen, a residual amount of neon is found in the plasma during seeding, presumably caused by residual gas in the seeding tubes from earlier experimental programs. Besides these two impurities whose densities are found to correlate with the seeding, carbon and oxygen, respectively originating from the first wall and residual water, were available for spectroscopic assessment. A total of four NBI blips at various levels of seeding flow give rise to four measurements. Changes in the impurity density levels are most prominent in the gases connected to the seeding. Due to the constant heating power at all four blips, the plasma profiles are found to be similar, giving rise
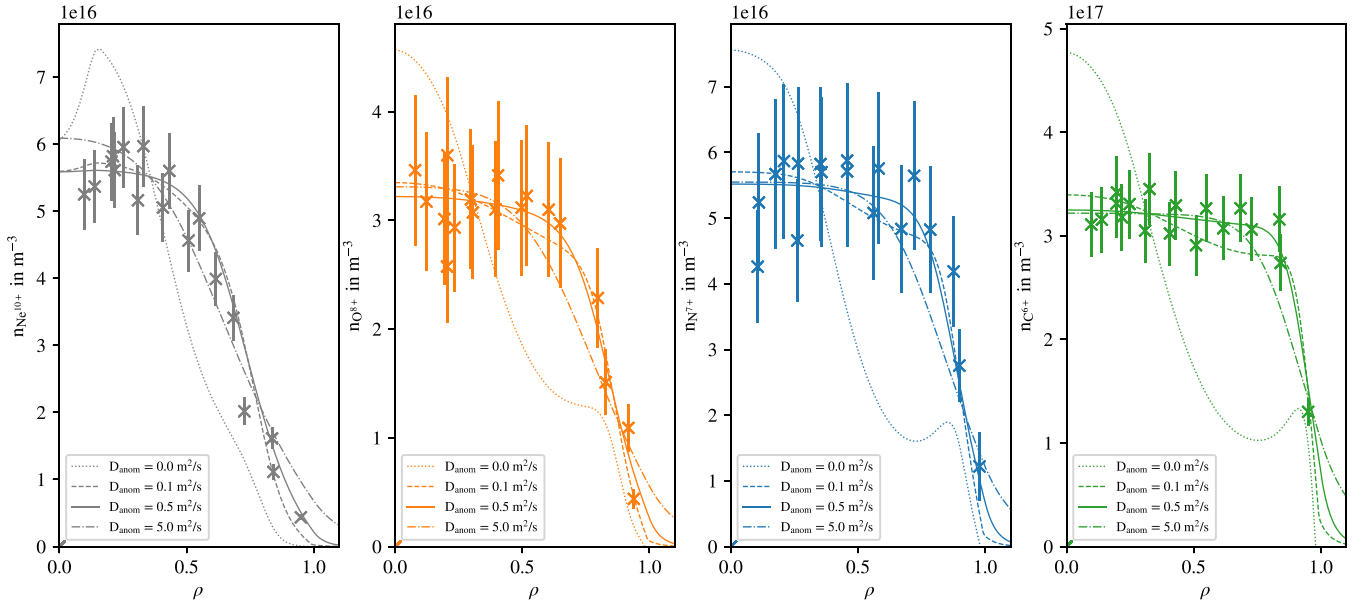
Figure 5. Radial density profiles of fully ionized neon, oxygen, nitrogen, and carbon (left-to-right) in case of the ECR heated program 20180920.049 measured using NBI blips. Data for oxygen and carbon are taken from the first blip, nitrogen from the second blip, and neon from the third blip. The experimental data points are accompanied by simulations of varying flat anomalous diffusion profiles.

to the expectation that the transport is similar at the four points in time. Based on this assumption, the transport properties are assessed jointly from data originating from different blips in the following.

The radial profiles of the assessed charge states of the impurities in figure 5 are similar. Uncertainties in the impurity densities represent the propagated errors in neutral density, rate data, and measured intensity. The profiles are flat near the magnetic axis and fall off at species dependent radial locations further out. The relative location of the gradient regions is consistent with higher Z impurities having higher ionization energies and subsequently being fully ionized further towards the plasma core only.

The measured data points are accompanied by one dimensional transport simulation results from pySTRAHL. The different line styles relate to simulations with varying levels of flat anomalous diffusion profiles added to the classical and neoclassical transport. The simulated density profiles are rescaled to match the average measured density inside $\rho = 0.5$. The introduction of a neutral density profile determined using the approach followed in [32] is found to have no significant influence on the impurity density profiles.

The comparison of purely (neo-)classical profiles with $D_{\text{anom}} = 0$ with the experimental profiles shows a clear mismatch due to the dominant neoclassical convection giving rise to centrally peaked impurity profiles. In contrast, all simulations with an anomalous diffusion exceeding $0.1 \, \text{m}^2 \, \text{s}^{-1}$ reproduce the general profile shape in the gradient region. Differences are present in form of the steepness in the gradient regions. In case of $D_{\text{anom}} \geqslant 5.0 \, \text{m}^2 \, \text{s}^{-1}$, the simulated gradient behaviour becomes significantly shallower than allowable within the experimental error bars, loosely restricting the anomalous diffusion level in ECRH discharges in W7-X to $D_{\text{anom}} \in [0.1, 5.0] \, \text{m}^2 \, \text{s}^{-1}$. With neoclassical diffusion and

convection levels of the order of $0.01 \, \text{m}^2 \, \text{s}^{-1}$ and $0.1 \, \text{m} \, \text{s}^{-1}$, respectively, the impurity transport in W7-X plasmas heated by ECRH is therefore dominated by anomalous diffusion.

The above described transport behaviour encloses the anomalous diffusion levels of $0.3 \, \text{m}^2 \, \text{s}^{-1}$ [30] and $0.5 \, \text{m}^2 \, \text{s}^{-1}$ [31] in the confined plasma region determined using LBO and TESPEL injection well. An edge peaking of the diffusion profiles as predicted by LBO is not reproduced by the CXRS based analysis. As apparent from the wide spread in the derived anomalous transport level, a CXRS based analysis conducted on stationary profiles can only restrict the anomalous transport level loosely when only accounting for a single ionization stage. The other diagnostics are more sensitive to the transport as they measure line emission in dynamically evolving situations. Altering the CXRS based analysis in ECRH plasmas to measure time dependent phenomena can be enabled by introducing a modulated impurity source [33, 34] which is foreseen in the next experimental campaign at W7-X. Alternatively, the measurement of multiple charge states of a single impurity allows to restrict the transport coefficients strongly [35].

5. Summary

A new analysis scheme for CXRS based impurity density measurements in W7-X using simulated neutral densities was introduced. The simulated neutral density was validated by comparison of experimental and synthetic BES signals and found to match the beam attenuation well in case of the three beam populations. The halo component was found to be systematically under-predicted by around 40%.

The localization of CXRS based ion temperature measurements using the three dimensional analysis grid was found to

be superior to a geometry based approach. The new localization was found to give rise to a more coherent localization of the related T_i measurements with poloidally oriented LoS being more strongly corrected. The absolute impurity density content derived from the CXRS measurements was compared to line integrated Z_{eff} as well as PHA data. A match of the effective plasma charge with both reference diagnostics was observed, validating the absolute impurity level determined by CXRS.

The particle transport properties in a typical ECRH discharge in W7-X were found to be governed by anomalous diffusion with D_{anom} being loosely constrained from $0.1\,\mathrm{m^2\,s^{-1}}$ to $5.0\,\mathrm{m^2\,s^{-1}}$ with no anomalous convection being observed. This level of anomalous transport is found to be consistent with results from LBO and TESPEL injection.

Data availability statement

The data cannot be made publicly available upon publication due to legal restrictions preventing unrestricted public distribution. The data that support the findings of this study are available upon reasonable request from the authors.

Acknowledgments

ORCID iDs

T Romba ⬢ https://orcid.org/0000-0002-2727-9385
F Reimold ⬢ https://orcid.org/0000-0003-4251-7924
R J E Jaspers ⬢ https://orcid.org/0000-0002-0589-7836
O P Ford ⬢ https://orcid.org/0000-0002-5646-4758
B Geiger ⬢ https://orcid.org/0000-0001-8706-1874
M Kubkowska ⬢ https://orcid.org/0000-0003-1320-7468
P Zs Poloskei ⬢ https://orcid.org/0000-0001-7781-5599
L Vanó ⬢ https://orcid.org/0000-0001-7883-6471

References

[1] Pütterich T 2005 Investigations of spectroscopic diagnostic of high-Z elements in fusion plasmas *PhD Thesis* Augsburg University

[2] Wegner T *et al* 2018 Design, capabilities and first results of the new laser blow-off system on Wendelstein 7-X *Rev. Sci. Instrum.* **89** 073505

[3] Bussiahn R, Tamura N, McCarthy K J, Burhenn R, Hayashi H, Laube R and Klinger T (LHD Experiment Group and W7-X Team) 2018 Tracer-encapsulated solid pellet (TESPEL) injection system for Wendelstein 7-X *Rev. Sci. Instrum.* **89** 10K112

[4] Pablant N A *et al* 2014 Measurement of core plasma temperature and rotation on W7-X made available by the x-ray imaging crystal spectrometer (XICS) *Technical Report* (Princeton, NJ: Princeton Plasma Physics Lab. (PPPL))

[5] Fonck R J, Darrow D S and Jaehnig K P 1984 Determination of plasma-ion velocity distribution via charge-exchange recombination spectroscopy *Phys. Rev.* A **29** 3288–309

[6] Erckmann V *et al* 1997 The W7-X project: scientific basis and technical realization *17th IEEE/NPSS Symp. Fusion Engineering (Cat. No. 97CH36131)* vol 1 (IEEE) pp 40–48

[7] Klinger T *et al* 2019 Overview of first Wendelstein 7-X high-performance operation *Nucl. Fusion* **59** 112004

[8] Ford O P *et al* 2020 Charge exchange recombination spectroscopy at Wendelstein 7-X *Rev. Sci. Instrum.* **91** 023503

[9] Vanó L 2022 Carbon content and transport investigations on Wendelstein 7-X with charge exchange recombination spectroscopy *PhD Thesis* University of Greifswald

[10] Churchill R M, Theiler C, Lipschultz B, Dux R, Pütterich T and Viezzer E (Alcator C-Mod Team and ASDEX Upgrade Team) 2013 Development of the gas puff charge exchange recombination spectroscopy (GP-CXRS) technique for ion measurements in the plasma edge *Rev. Sci. Instrum.* **84** 093505

[11] von Hellermann M, Breger P, Frieling J, Konig R, Mandl W, Maas A and Summers H P 1995 Analytical approximation of cross-section effects on charge exchange spectra observed in hot fusion plasmas *Plasma Phys. Control. Fusion* **37** 71

[12] Duesing G, Altmann H, Falter H, Goede A, Haange R, Hemsworth R S, Kupschus P, Stork D and Thompson E 1987 Neutral beam injection system *Fusion Technol.* **11** 163–202

[13] Spanier A *et al* 2021 Performance of the first neutral beam injector at the Wendelstein 7-X stellarator *Fusion Eng. Des.* **163** 112115

[14] McDermott R M *et al* 2018 Evaluation of impurity densities from charge exchange recombination spectroscopy measurements at ASDEX upgrade *Plasma Phys. Control. Fusion* **60** 095007

[15] von Hellermann M G, Delabie E, Jaspers R J E, Biel W, Marchuk O, Summers H P, Whiteford A, Giroud C, Hawkes N C and Zastrow K D 2008 Active beam spectroscopy *AIP Conf. Proc.* **988** 165–76

[16] Geiger B *et al* 2020 Progress in modelling fast-ion d-alpha spectra and neutral particle analyzer fluxes using FIDASIM *Plasma Phys. Control. Fusion* **62** 105008

[17] Swee C, Geiger B, Dux R, Kumar S T A, Castillo J F, Bader A and Gerard M 2021 Impurity transport studies at the HSX stellarator using active and passive CVI spectroscopy *Plasma Phys. Control. Fusion* **64** 015008

[18] Heimann P, Bluhm T, Ch Hennig H K, Kühner G, Maier J, Riemann H and Zilker M 2008 Database structures and interfaces for W7-X *Fusion Eng. Des.* **83** 393–6

[19] Bozhenkov S A *et al* 2017 The Thomson scattering diagnostic at Wendelstein 7-X and its performance in the first operation phase *J. Instrum.* **12** P10004

[20] Nadaraya E A 1964 On estimating regression *Theory Probab. Appl.* **9** 141–2

[21] McDermott R M, Dux R, Guzman F, Pütterich T, Fischer R and Kappatou A (The ASDEX Upgrade Team) 2020 Development of Ar^{16+} charge exchange recombination

spectroscopy measurements at ASDEX Upgrade *Nucl. Fusion* **61** 016019

[22] Jaspers R J E *et al* 2012 A high etendue spectrometer suitable for core charge eXchange recombination spectroscopy on ITER *Rev. Sci. Instrum.* **83** 10D515

[23] Beurskens M N A *et al* 2021 Ion temperature clamping in Wendelstein 7-X electron cyclotron heated plasmas *Nucl. Fusion* **61** 116072

[24] Pavone A *et al* 2019 Measurements of visible bremsstrahlung and automatic Bayesian inference of the effective plasma charge Zeff at W7-X *J. Instrum.* **14** C10003

[25] Kubkowska M *et al* 2018 First results from the soft x-ray pulse height analysis system on Wendelstein 7-X stellarator *Fusion Eng. Des.* **136** 58–62

[26] Smith H 2022 Neotransp (available at: https://gitlab.mpcdf. mpg.de/smithh/neotransp)

[27] Hirshman S P, Shaing K C, van Rij W I, Beasley C O Jr and Crume E C Jr 1986 Plasma transport coefficients for nonsymmetric toroidal confinement systems *Phys. Fluids* **29** 2951–9

[28] Van Rij W I and Hirshman S P 1989 Variational bounds for transport coefficients in three-dimensional toroidal plasmas *Phys. Fluids* B **1** 563–9

[29] Langenberg A *et al* 2020 Charge-state independent anomalous transport for a wide range of different impurity species observed at Wendelstein 7-X *Phys. Plasmas* **27** 052510

[30] Geiger B *et al* 2019 Observation of anomalous impurity transport during low-density experiments in W7-X with laser blow-off injections of iron *Nucl. Fusion* **59** 046009

[31] Bussiahn R *et al* 2021 Impurity transport studies on Wendelstein 7-X by tracer-encapsulated solid pellets *47th EPS Conf. on Plasma Physics* (European Physical Society)

[32] Fujii K, Goto M and Morita S (LHD Experiment Group) 2015 Study of neutral hydrogen transport in LHD core plasmas based on high dynamic-range Balmer-α spectroscopy *Nucl. Fusion* **55** 063029

[33] Takenaga H, Nagashima K, Sakasai A, Oikawa T and Fujita T 1998 Determination of particle transport coefficients in reversed shear plasma of JT-60U *Plasma Phys. Control. Fusion* **40** 183

[34] Takenaga H *et al* 1999 Particle confinement and transport in JT-60U *Nucl. Fusion* **39** 1917

[35] Nishizawa T *et al* 2022 Non-parametric inference of impurity transport coefficients in the ASDEX Upgrade tokamak *Nucl. Fusion* **62** 076021